Dipole-assisted thermotics: Experimental demonstration of dipole-driven thermal invisibility

Liujun Xu, Shuai Yang, and Jiping Huang [*]

*Department of Physics, State Key Laboratory of Surface Physics, and Key Laboratory of Micro
and Nano Photonic Structures (MOE), Fudan University, Shanghai 200438, China*

Thermal management has made considerable progress in the past decade for the emerging field of thermal metamaterials. However, two severe problems still handicap the development of thermal metamaterials. That is, thermal conductivities should be singular and uncommon as required by corresponding theories. To solve these problems, here we establish the theory of dipole-assisted thermotics. By tailoring the thermal dipole moment, thermal invisibility can be achieved without the requirements of singular and uncommon thermal conductivities. Furthermore, finite-element simulations and laboratory experiments both validate the theoretical analyses. The performance of the dipole-driven scheme is excellent in both two and three dimensions, and in both steady and transient states. Dipole-assisted thermotics not only offers a distinct mechanism to achieve thermal invisibility, but also has potential applications in thermal management such as infrared signature reduction, thermal protection, and infrared camouflage.

I. INTRODUCTION

With growing concerns about energy issues, many researchers have focused their research interest on thermal management. This trend was mainly driven by the emerging field of thermal metamaterials in the past decade. The most representative example is thermal invisibility [1–17], which has almost run through the development of thermal metamaterials. Thermal invisibility is characterized by the uniform thermal field of the matrix. For this purpose, many schemes have been proposed, but they have their own shortcomings. The initial exploration is based on transformation thermotics [1–5], which is a thermal counterpart of transformation optics [18]. However, transformation thermotics leads to four severe problems, thus limiting practical applications. The first is anisotropy, which requires different radial and tangential components of a tensorial thermal conductivity. The second is inhomogeneity, which means a spatially distributed thermal conductivity. The third is singularity, which takes zero and infinite thermal conductivities. The fourth is uncommon thermal conductivities. Thermal conductivities of common materials range only from 0.026 (air) to 430 W m^{-1} K^{-1} (silver), and those out of this range are uncommon [15]. Although highly conductive materials do exist such as carbon nanotubes and graphene, they are rare and practically difficult to utilize, thus remaining a problem.

Although these four problems restrict practical applications, they also promote the development of thermal metamaterials by solving them. Fortunately, the problems of anisotropy and inhomogeneity were solved soon [6–15]. However, the problems of singular and uncommon thermal conductivities still cannot be solved simultaneously. For example, we discuss a matrix with a very high thermal conductivity, such as copper (400 W m^{-1} K^{-1}), because high thermal conductivities correspond to the high efficiency of heat transfer. When a bilayer cloak [6–11] is designed, thermal conductivities of the inner and outer shells are, respectively, 0 and 2615 W m^{-1} K^{-1}, which are singular and uncommon [see Fig. 1(a)]. When the concept of neutral inclusion [11–14] is used, the thermal conductivity of the shell should be 727 W m^{-1} K^{-1}, which is also uncommon [see Fig. 1(b)]. When a near-zero-index cloak [15] is designed, the thermal conductivity of the inner shell should tend to infinity, which is singular [see Fig. 1(c)]. These two problems (singular and uncommon thermal conductivities) largely restrict the development of thermal metamaterials because they require either complex structures or rare materials. For example, for the realization of infinite thermal conductivities, thermal convection should be introduced based on complex structures [15].

To completely solve these two problems, here we propose the theory of dipole-assisted thermotics, which can remove the requirements of singular and uncommon thermal conductivities simultaneously. In fact, we do not even require the design of a shell, and a thermal dipole is enough [see Fig. 1(d)]. This lies in the particularity of the thermal field of a thermal dipole, which can just offset the influence of a particle by designing the thermal dipole moment (M). It should be mentioned that, although the dipole-driven scheme removes the requirements of singular and uncommon thermal conductivities, the essence of this work is about macroscopic thermal processes rather than thermal conductivities.

In what follows, we establish the theory of dipole-assisted thermotics in two dimensions. Furthermore, the theory is validated by finite-element simulations and laboratory experiments. Finally, we present the three-dimensional results including the theory and finite-element simulations.
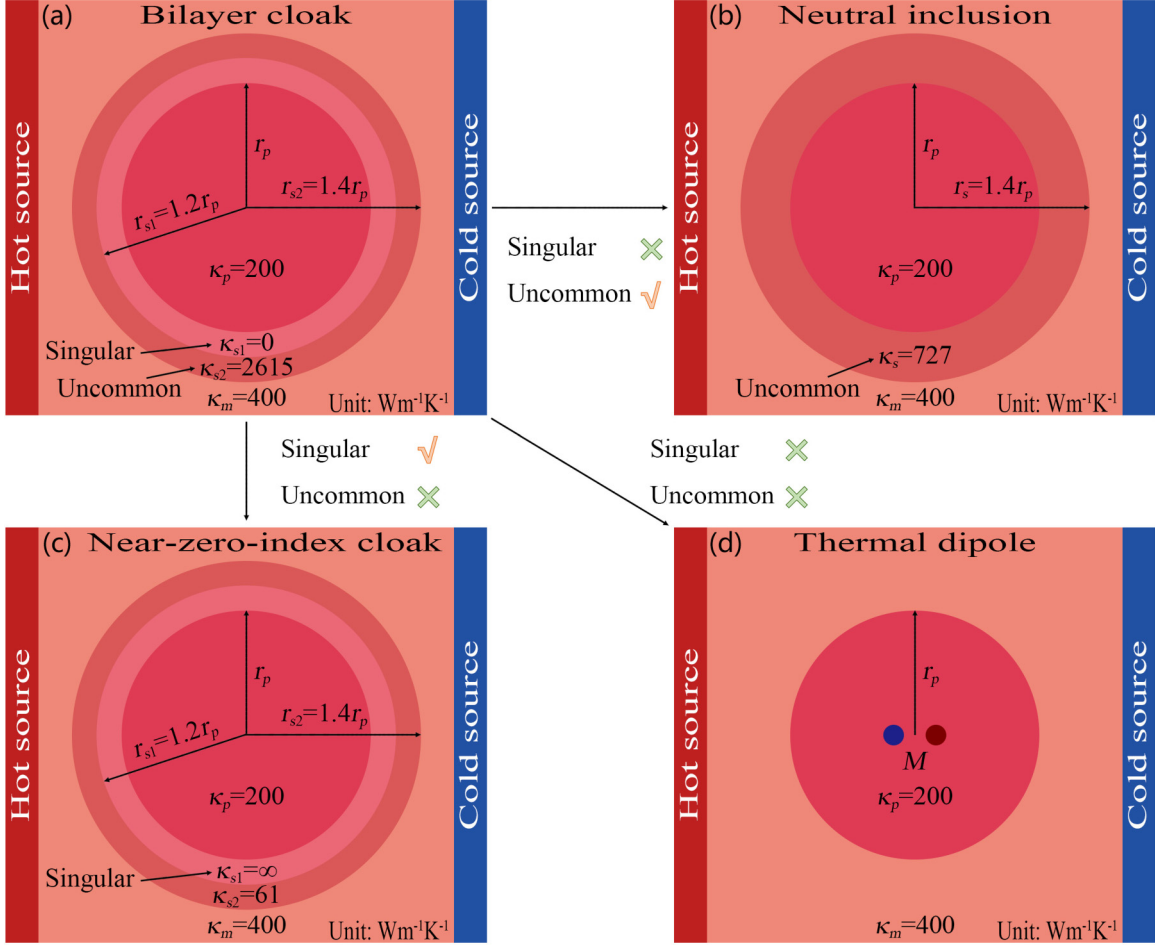
[*]jphuang@fudan.edu.cn

FIG. 1. Different approaches to thermal invisibility. (a) A bilayer cloak satisfying $\kappa_m = \kappa_{s2}(1-p)/(1+p)$, where $p = (r_{s1}/r_{s2})^2$. (b) The concept of neutral inclusion satisfying $\kappa_m = \kappa_s[\kappa_p + \kappa_s + (\kappa_p - \kappa_s)p]/[\kappa_p + \kappa_s - (\kappa_p - \kappa_s)p]$, where $p = (r_p/r_s)^2$. (c) A near-zero-index cloak satisfying $\kappa_m = \kappa_{s2}(1+p)/(1-p)$, where $p = (r_{s1}/r_{s2})^2$. (d) A thermal dipole proposed in this work. Clearly, none of these approaches can simultaneously remove the requirements of singular and uncommon thermal conductivities except for the present dipole-driven scheme.

II. THEORY OF DIPOLE-ASSISTED THERMOTICS IN TWO DIMENSIONS

Thermal invisibility aims to keep the matrix thermal field undistorted, and hence we focus on the matrix thermal field in what follows. In the presence of an external uniform thermal field G_0, when there is a particle (with thermal conductivity κ_p and radius r_p) embedded in the matrix (with thermal conductivity κ_m), it will distort the matrix thermal field. The matrix thermal field (generated by the external uniform thermal field), denoted as G_{me}, can be expressed as

$$G_{me} = -\nabla T_{me}. \tag{1}$$

T_{me} is the temperature distribution given by [19]

$$T_{me} = -G_0 r \cos\theta - \frac{\kappa_m - \kappa_p}{\kappa_m + \kappa_p} r_p^2 G_0 r^{-1} \cos\theta + T_0, \tag{2}$$

where (r, θ) denote the cylindrical coordinates whose origin is in the center of the particle, $G_0 = |G_0|$, and T_0 is the temperature at $\theta = \pm\pi/2$.

When there is only a thermal dipole (with heater power Q and distance l) in the center of the particle, it will generate a thermal field in the matrix. The matrix thermal field

(generated by the thermal dipole), denoted as G_{md}, can be expressed as

$$G_{md} = -\nabla T_{md}. \tag{3}$$

T_{md} is the temperature distribution given by

$$T_{md} = \frac{M}{\pi(\kappa_m + \kappa_p)} r^{-1} \cos\theta + T_0, \tag{4}$$

where M is the thermal dipole moment given by $M = Ql$. Equation (4) is valid when $r \gg l$, which is investigated in the discussion section. Detailed derivations of Eq. (4) are as follows. In passive regions, we can write down the general solution [19] to the heat conduction equation $\nabla \cdot (-\kappa \nabla T) = 0$,

$$T = A_0 + B_0 \ln r + \sum_{i=1}^{\infty} [A_i \sin(i\theta) + B_i \cos(i\theta)]r^i$$

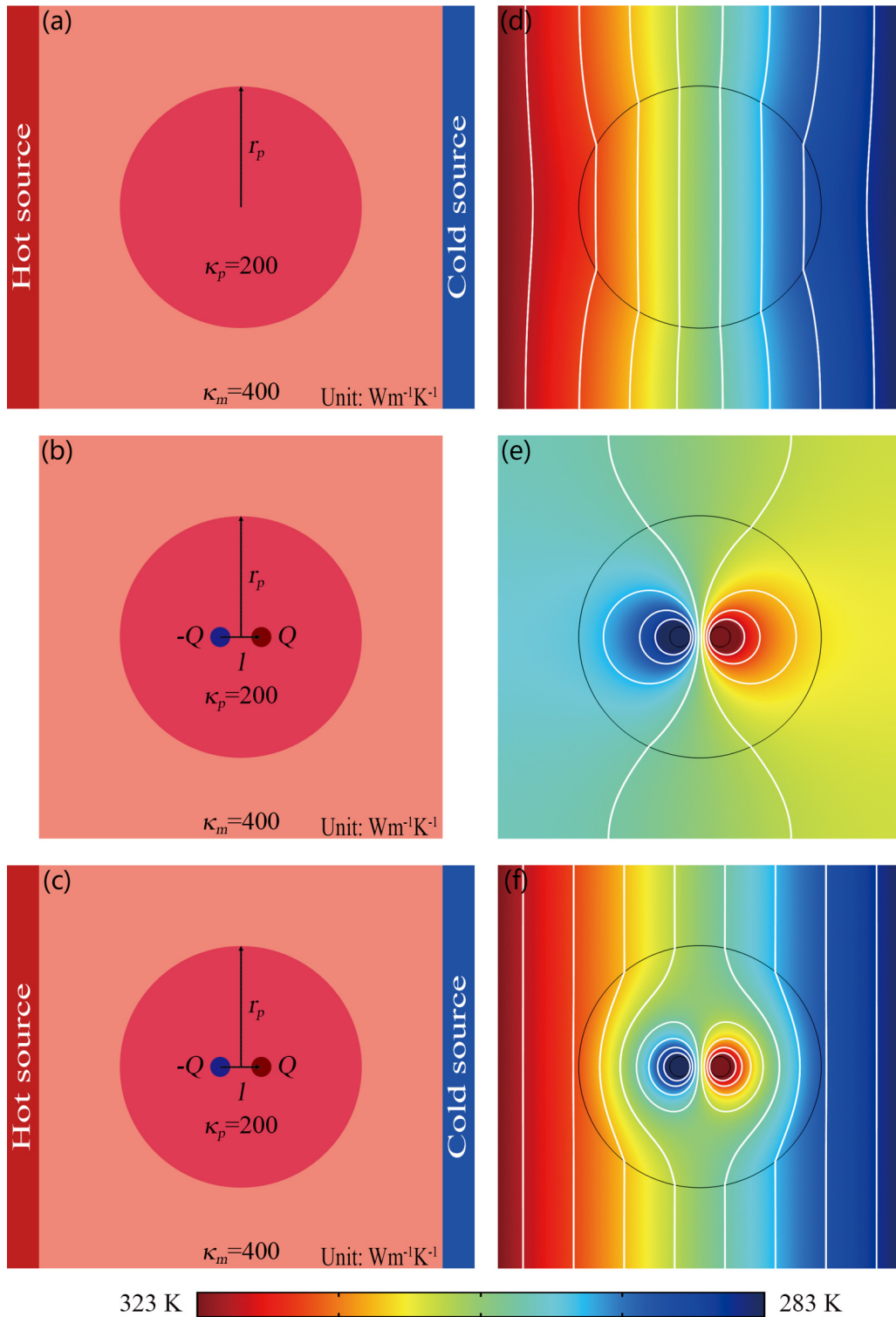$$+ \sum_{j=1}^{\infty} [C_j \sin(j\theta) + D_j \cos(j\theta)]r^{-j}. \tag{5}$$

FIG. 2. Finite-element simulations in the presence of (a, d) an external uniform thermal field, (b, e) a thermal dipole, and (c, f) an external uniform thermal field and a thermal dipole together. The simulation box is 20×20 cm^2, $r_p = 6$ cm, and $l = 2$ cm. The thermal conductivities of the particle and the matrix are 200 and 400 W m^{-1} K^{-1}, respectively. The thermal dipole moment should be 452.4 W m as required by Eq. (16), which leads to $Q = 22620$ W. The heater or cooler of the thermal dipole has a radius of 0.5 cm. White lines represent isotherms. For the convenience of comparison, temperatures higher than 323 K are shown as 323 K, and temperatures lower than 283 K are shown as 283 K.

Boundary conditions are given by the continuous temperatures and normal heat fluxes,

$$T_{pd}(r_p) = T_{md}(r_p), \qquad (6)$$

$$(-\kappa_p \partial T_{pd}/\partial r)_{r_p} = (-\kappa_m \partial T_{md}/\partial r)_{r_p}, \qquad (7)$$

where T_{pd} and T_{md} are the temperature distributions (generated by the thermal dipole) of the particle and matrix, respectively.

We perform some limit analyses to determine the forms of T_{pd} and T_{md}. We suppose $r_p \to \infty$, and then the particle temperature distribution (generated by the thermal dipole) can be expressed as

$$
\begin{aligned}
T_{pd}(r_p \to \infty) &= \frac{-Q}{2\pi\kappa_p}\ln r_+ + \frac{Q}{2\pi\kappa_p}\ln r_- \\
&= \frac{Ql}{2\pi\kappa_p}r^{-1}\cos\theta \\
&= \frac{M}{2\pi\kappa_p}r^{-1}\cos\theta,
\end{aligned} \qquad (8)
$$

where r_+ and r_- are the distances to the heater and cooler of the dipole, respectively. Equation (8) is valid when $r \gg l$ (or $l \to 0$). Thus, the temperature distribution of a thermal dipole in two dimensions is characterized by $r^{-1}\cos\theta$.

We further consider a finite r_p. The matrix temperature distribution should also have the property of $r^{-1}\cos\theta$, but certainly with a different coefficient from Eq. (8). The particle temperature distribution has two components. One is determined by Eq. (8), and the other is a uniform thermal field generated by the "thermal polarization." These can be concluded as

$$T_{pd} = \frac{M}{2\pi\kappa_p}r^{-1}\cos\theta + \alpha r\cos\theta + T_0, \qquad (9)$$

$$T_{md} = \beta r^{-1}\cos\theta + T_0. \qquad (10)$$

Solving Eqs. (6), (7), (9), and (10), the undetermined coefficients can be derived:

$$\alpha = \frac{-M(\kappa_m - \kappa_p)}{2\pi r_p^2 \kappa_p(\kappa_m + \kappa_p)}, \qquad (11)$$

$$\beta = \frac{M}{\pi(\kappa_m + \kappa_p)}. \qquad (12)$$

With Eq. (12), Eq. (10) turns to the form of Eq. (4).

Because of the superposition principle of vector fields, the matrix thermal field (generated by the external uniform thermal field and thermal dipole together), denoted as G_s, can be expressed as

$$G_s = G_{me} + G_{md} = -\nabla T_s. \qquad (13)$$

T_s is the temperature distribution given by

$$
\begin{aligned}
T_s = &-G_0 r\cos\theta - \left(\frac{\kappa_m - \kappa_p}{\kappa_m + \kappa_p}r_p^2 G_0 - \frac{M}{\pi(\kappa_m + \kappa_p)}\right)r^{-1}\cos\theta \\
&+ T_0.
\end{aligned} \qquad (14)
$$

As mentioned at the very beginning, thermal invisibility is characterized by the undistorted thermal field of the matrix, and thus the second term on the right-hand side of Eq. (14) should be zero:

$$\frac{\kappa_m - \kappa_p}{\kappa_m + \kappa_p}r_p^2 G_0 - \frac{M}{\pi(\kappa_m + \kappa_p)} = 0. \qquad (15)$$

Solving Eq. (15), we can derive the thermal dipole moment,

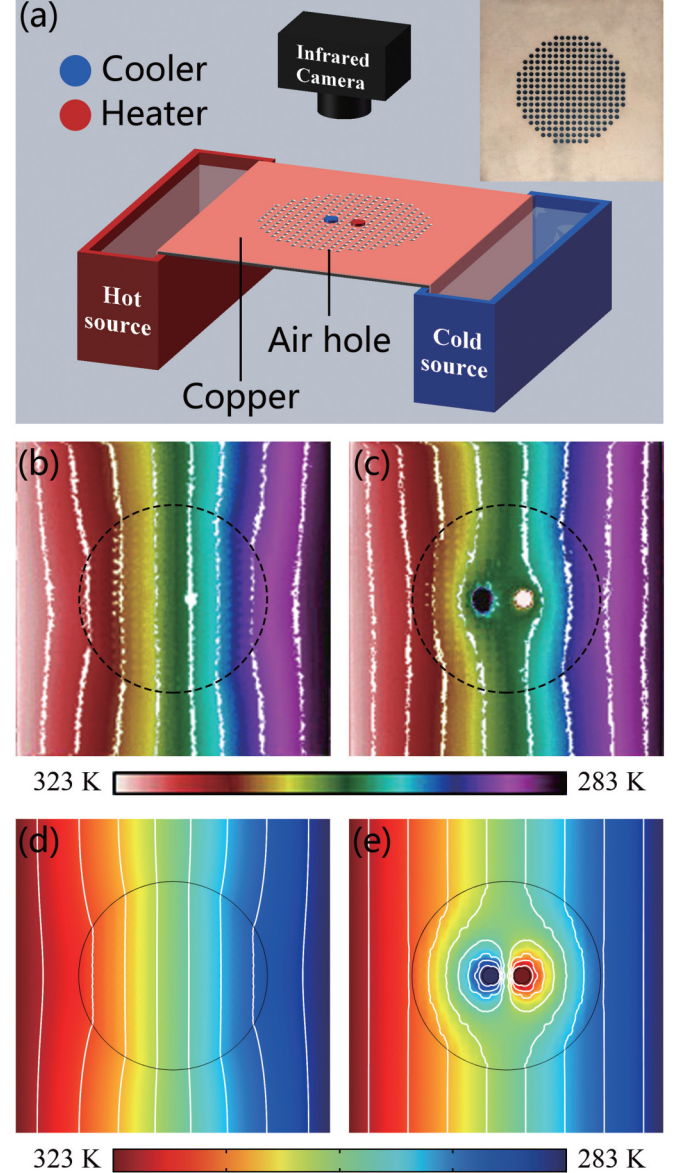$$M = (\kappa_m - \kappa_p)f G_0, \qquad (16)$$

FIG. 3. Laboratory experiments. (a) Schematic diagrams of the experimental devices and the fabricated sample. (b, c) Measured results without and with a thermal dipole, respectively. (d, e) Corresponding finite-element simulations based on the experimental settings in (a). Copper: thermal conductivity 400 W m^{-1} K^{-1}, density 8960 kg m^{-3}, and heat capacity 385 J kg^{-1} K^{-1}. Air: thermal conductivity 0.026 W m^{-1} K^{-1}, density 1.29×10^{-3} kg m^{-3}, and heat capacity 1005 J kg^{-1} K^{-1}. The radius of the 256 air holes is 0.22 cm, and the distance between air holes is 2/3 cm.

where $f = \pi r_p^2$ is the acreage of the particle. When the thermal dipole moment is set as required by Eq. (16), thermal invisibility can be achieved.

III. FINITE-ELEMENT SIMULATIONS IN TWO DIMENSIONS

Further, we perform finite-element simulations with COMSOL MULTIPHYSICS [20] to validate the theoretical analyses. In Figs. 2(a) and 2(d), the temperatures of the left and right boundaries are set at 323 and 283 K, and the upper and lower boundaries are insulated. If there is a particle with different thermal conductivity from the matrix in the center, the isotherms are contracted due to the smaller thermal conductivity of the particle [see Fig. 2(d)]. The distorted temperature profile makes the particle visible with infrared detection. Then, we explore the thermal profile of a thermal dipole [see Figs. 2(b) and 2(e)]. All boundaries are insulated, and we set the temperature at $\theta = \pm \pi/2$ at 303 K as a reference temperature. The temperature profile is presented in Fig. 2(e). Finally, we combine the structures shown in Figs. 2(a) and 2(b) together and obtain the expected structure as presented in Fig. 2(c). As predicted by Eq. (16), the distorted temperature profile can be restored [see Fig. 2(f)]. Therefore, the particle becomes invisible with infrared detection, and thermal invisibility is achieved with a thermal dipole.

IV. LABORATORY EXPERIMENTS IN TWO DIMENSIONS

We also perform laboratory experiments to validate the theoretical analyses and finite-element simulations. We fabricate the sample based on a copper plate (400 W m^{-1} K^{-1}). Air holes (0.026 W m^{-1} K^{-1}) are engraved on the copper plate via laser cut, which makes the effective thermal conductivity of the corresponding region 200 W m^{-1} K^{-1} [see the inset in Fig. 3(a)]. The upper and lower surfaces are, respectively, covered with transparent plastic and foamed plastic (which are both insulated) to reduce the negative effects of infrared reflection and thermal convection.

The designed power of the thermal dipole is 22 620 W for the heater and $-22\,620$ W for the cooler, which is an extremely large value. On the one hand, it maintains the uniform thermal field of the matrix. On the other hand, it generates a higher (or lower) temperature inside the heater (or cooler) than the hot (or cold) source. However, the higher (or lower) temperature inside the heater (or cooler) does not contribute to the effect of thermal invisibility because only the edge temperature of the heater (or cooler) makes sense. Such a statement can be understood by the uniqueness theorem in thermotics [21]. Therefore, we require only to keep the temperature of the heater (or cooler) at 325 (or 281) K to achieve thermal invisibility as ensured by the uniqueness theorem in thermotics. The two temperatures can be directly
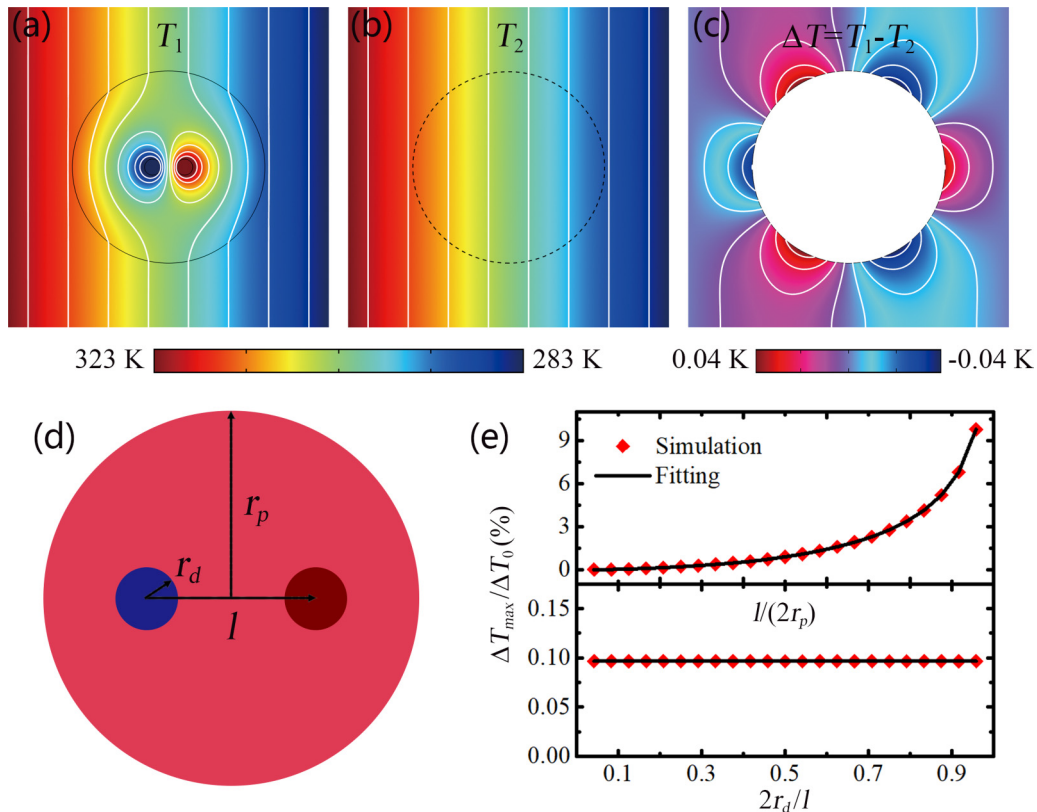

FIG. 4. Effects of the thermal dipole on thermal invisibility. (a) The dipole-driven temperature distribution. (b) The temperature distribution when the thermal conductivities of the matrix and particle are the same (say, 400 W m^{-1} K^{-1}). (c) The matrix temperature-difference distribution. In (d) and (e), we explore the effects of two parameters (l and r_d) on thermal invisibility. The upper panel in (e) is with $r_d = 0$ cm, say, point heater and cooler of the dipole. The lower panel in (e) is with $l = 2$ cm.

obtained from the finite-element simulation [Fig. 2(f)], and they are dependent on the radius of the heater (or cooler). Thus, the thermal dipole can be realized by a ceramic heater and an ice-water bag. Since the heat capacity of water is 4.2×10^3 J kg^{-1} K^{-1} (a very large value), it can maintain a constant temperature for several minutes, which is enough for our steady experiments.

We measure the sample between the hot source (323 K) and the cold source (283 K) with a Flir E60 infrared camera. The measured results without and with a thermal dipole are presented in Figs. 3(b) and 3(c), respectively. We also perform finite-element simulations based on the structure presented in Fig. 3(a), and set the thermal dipole at two constant temperatures [see Figs. 3(d) and 3(e)]. The experimental results [Figs. 3(b) and 3(c)] and finite-element simulations [Figs. 2(d), 2(f), 3(d), and 3(e)] both validate that the thermal dipole is reliable and flexible to achieve thermal invisibility.

V. DISCUSSIONS OF THE TWO-DIMENSIONAL RESULTS

There is only one approximation (say, $r \gg l$) in the whole process to ensure the validity of Eq. (4). Therefore, we discuss the effect of this approximation on thermal invisibility. We compare our dipole-driven result [Fig. 4(a), whose parameters are the same as those for Fig. 2(f)] with a reference [Fig. 4(b)]. Clearly, the matrix temperature distributions are totally the same. We also plot the matrix temperature-difference distribution ($\Delta T = T_1 - T_2$) to present quantitative analyses [see Fig. 4(c)]. The maximum value of the temperature difference ($\Delta T_{\max}$) is 0.04 K. Compared with the temperature difference between the hot and cold sources ($\Delta T_0 = 40$ K), the relative error ($\Delta T_{\max}/\Delta T_0$) is only 0.1%, which shows the excellent performance of the dipole-driven scheme.

Clearly, relative errors can reflect the effect of the thermal dipole on thermal invisibility. Therefore, we calculate $\Delta T_{\max}/\Delta T_0$ with different r_d (the radius of the heater or cooler) and l (the distance between the heater and cooler) [Fig. 4(d)], and plot two curves showing $\Delta T_{\max}/\Delta T_0$ changing with $l/(2r_p)$ and $2r_d/l$ [Fig. 4(e)]. The upper curve in Fig. 4(e) shows that the performance of the thermal dipole decreases with the increment of $l/(2r_p)$. When $l/(2r_p) \to 0$ (say, $l \to 0$), $\Delta T_{\max}/\Delta T_0 \to 0$, which indicates the perfect performance. However, the lower curve in Fig. 4(e) shows that the performance of the thermal dipole remains unchanged with the increment of $2r_d/l$. Therefore, only one parameter (say, the distance l) mainly affects the effect of the thermal dipole on thermal invisibility, and the shorter is the better.

We also perform transient simulations based on the experimental settings presented in Fig. 3(a) [see Fig. 5]. The transient behavior is good when the initial temperature is set at the middle temperature of the hot and cold sources. Figures 5(a)–5(d) are references without a thermal dipole. The distorted matrix isotherms make the particle in the center visible. By contrast, the straight matrix isotherms in Figs. 5(e)–5(h) demonstrate that the thermal dipole can realize thermal invisibility in transient regimes.
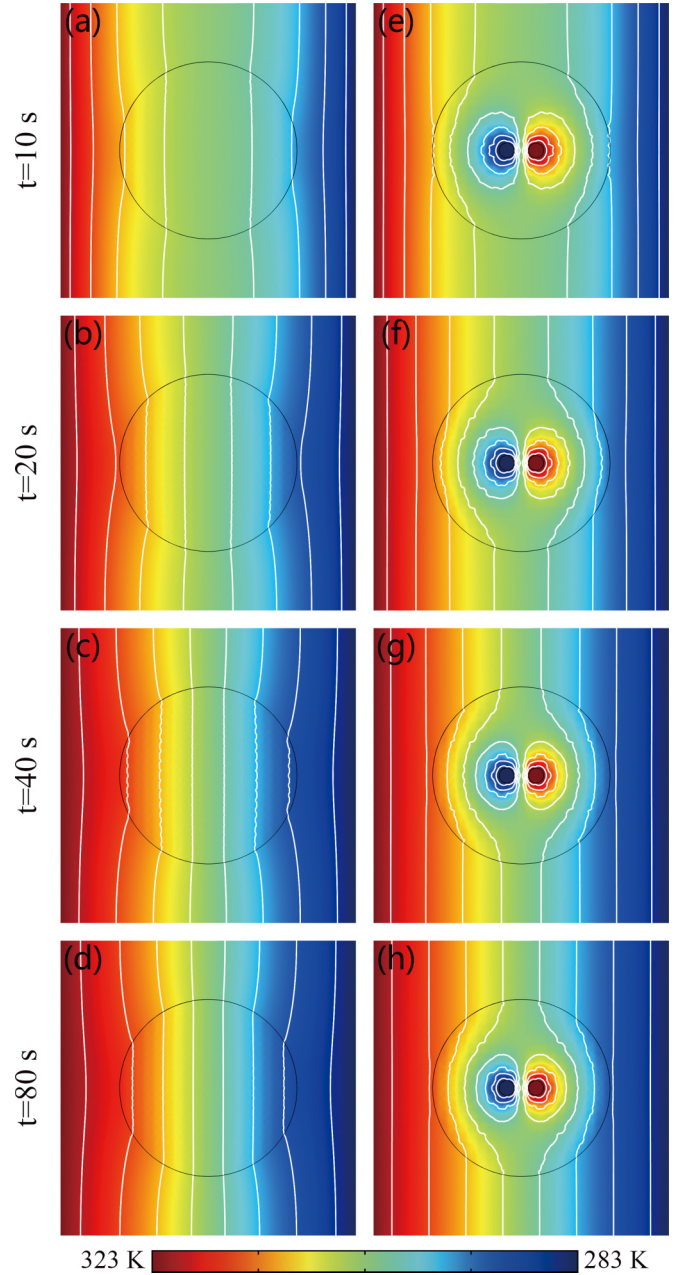

FIG. 5. Transient simulations based on the structure presented in Fig. 3(a). The heater and cooler of the thermal dipole are set at constant temperatures as applied in experiments. Results (a–d) without and (e–h) with the thermal dipole, respectively. The initial temperature is set at 303 K.

VI. RESULTS IN THREE DIMENSIONS

In what follows, we use primes to denote three dimensions. The matrix thermal field (generated by the external uniform thermal field $\mathbf{G}'_0$), denoted as $\mathbf{G}'_{me}$, can be expressed as

$$\mathbf{G}'_{me} = -\nabla T'_{me}. \tag{17}$$

T'_{me} is the temperature distribution given by [19]

$$T'_{me} = -G'_0 r \cos\theta - \frac{\kappa'_m - \kappa'_p}{2\kappa'_m + \kappa'_p} r'^3_p G'_0 r^{-2} \cos\theta + T'_0. \tag{18}$$
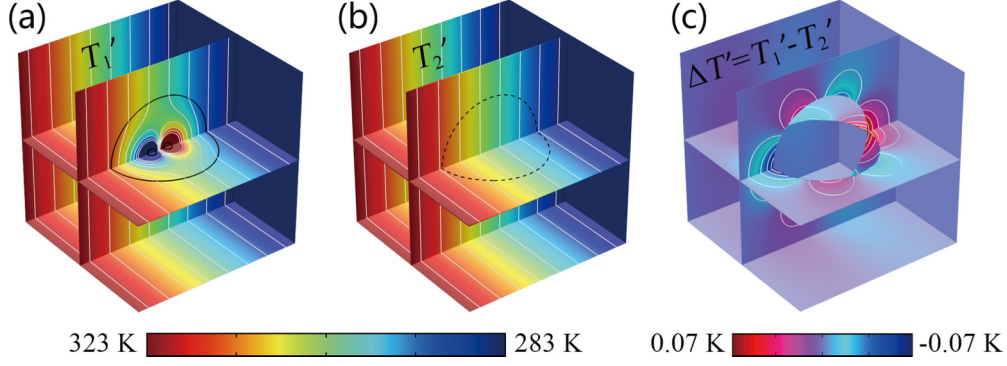
FIG. 6. Finite-element simulations in three dimensions. The simulation box is $20 \times 20 \times 20$ cm^3; $r'_p = 6$ cm and $l' = 2$ cm. The thermal conductivities of the particle and the matrix in (a) are 200 and 400 W m^{-1} K^{-1}, respectively, and those in (b) are the same (say, 400 W m^{-1} K^{-1}) for comparison. The thermal dipole moment in (a) should be 36.2 W m as required by Eq. (30), which leads to $Q' = 1810$ W. The heater and cooler of the thermal dipole have a radius 0.5 cm. The temperatures of the hot source and the cold source are set at 323 and 283 K. (c) The matrix temperature-difference distribution.

The matrix thermal field (generated by the thermal dipole), denoted as $\boldsymbol{G}'_{md}$, can be expressed as

$$\boldsymbol{G}'_{md} = -\nabla T'_{md}. \tag{19}$$

T'_{md} is the temperature distribution given by

$$T'_{md} = \frac{3M'}{4\pi(2\kappa'_m + \kappa'_p)} r^{-2} \cos\theta + T'_0. \tag{20}$$

Detailed derivations of Eq. (20) are as follows. The general solution to the heat conduction equation in three dimensions is [19]

$$T = \sum_{i=0}^{\infty}(A_i r^{-1/2+\sqrt{1/4+i(i+1)}} + B_i r^{-1/2-\sqrt{1/4+i(i+1)}})P_i(\cos\theta), \tag{21}$$

where P_i is the Legendre polynomial. The boundary conditions are given by the continuous temperatures and heat fluxes, which have the same mathematical forms as Eqs. (6) and (7). We perform similar limit analyses to determine the forms of T'_{pd} and T'_{md}. We suppose $r'_p \to \infty$, and then the particle temperature distribution (generated by the thermal dipole) in three dimensions can be expressed as

$$T'_{pd}(r'_p \to \infty) = \frac{Q'}{4\pi\kappa'_p} r'^{-1}_+ + \frac{-Q'}{4\pi\kappa'_p} r'^{-1}_- = \frac{Q'l'}{4\pi\kappa'_p} r^{-2} \cos\theta$$

$$= \frac{M'}{4\pi\kappa'_p} r^{-2} \cos\theta. \tag{22}$$

Equation (22) is valid only when $r \gg l'$ (or $l' \to 0$). The temperature distribution of a thermal dipole in three dimensions is characterized by $r^{-2} \cos\theta$. We further consider a finite r'_p. Similar to the analyses in two dimensions, T'_{pd} and T'_{md} can be concluded as

$$T'_{pd} = \frac{M'}{4\pi\kappa'_p} r^{-2} \cos\theta + \alpha' r \cos\theta + T'_0, \tag{23}$$

$$T'_{md} = \beta' r^{-2} \cos\theta + T'_0. \tag{24}$$

Solving Eqs. (6), (7), (23), and (24), the undetermined coefficients can be derived:

$$\alpha' = \frac{-M'(\kappa'_m - \kappa'_p)}{2\pi r'^3_p \kappa'_p(2\kappa'_m + \kappa'_p)}, \tag{25}$$

$$\beta' = \frac{3M'}{4\pi(2\kappa'_m + \kappa'_p)}. \tag{26}$$

With Eq. (26), Eq. (24) turns to the form of Eq. (20).

Because of the superposition principle, the matrix thermal field (generated by the external uniform thermal field and the thermal dipole together), denoted as $\boldsymbol{G}'_s$, can be expressed as

$$\boldsymbol{G}'_s = \boldsymbol{G}'_{me} + \boldsymbol{G}'_{md} = -\nabla T'_s. \tag{27}$$

T'_s is the temperature distribution given by

$$T'_s = -G'_0 r \cos\theta$$
$$- \left[\frac{\kappa'_m - \kappa'_p}{2\kappa'_m + \kappa'_p} r'^3_p G'_0 - \frac{3M'}{4\pi(2\kappa'_m + \kappa'_p)}\right] r^{-2} \cos\theta + T'_0. \tag{28}$$

Thermal invisibility requires the second term on the right-hand side of Eq. (28) to be zero:

$$\frac{\kappa'_m - \kappa'_p}{2\kappa'_m + \kappa'_p} r'^3_p G'_0 - \frac{3M'}{4\pi(2\kappa'_m + \kappa'_p)} = 0. \tag{29}$$

Solving Eq. (29), we can derive the thermal dipole moment,

$$M' = (\kappa'_m - \kappa'_p)f'G'_0, \tag{30}$$

where $f' = 4\pi r'^3_p/3$ is the volume of the particle.

We also perform finite-element simulations in three dimensions. We compare the dipole-driven result [Fig. 6(a)] with a reference [Fig. 6(b)]. The same matrix temperature distributions indicate the feasibility of realizing thermal invisibility with a thermal dipole in three dimensions. We also plot the
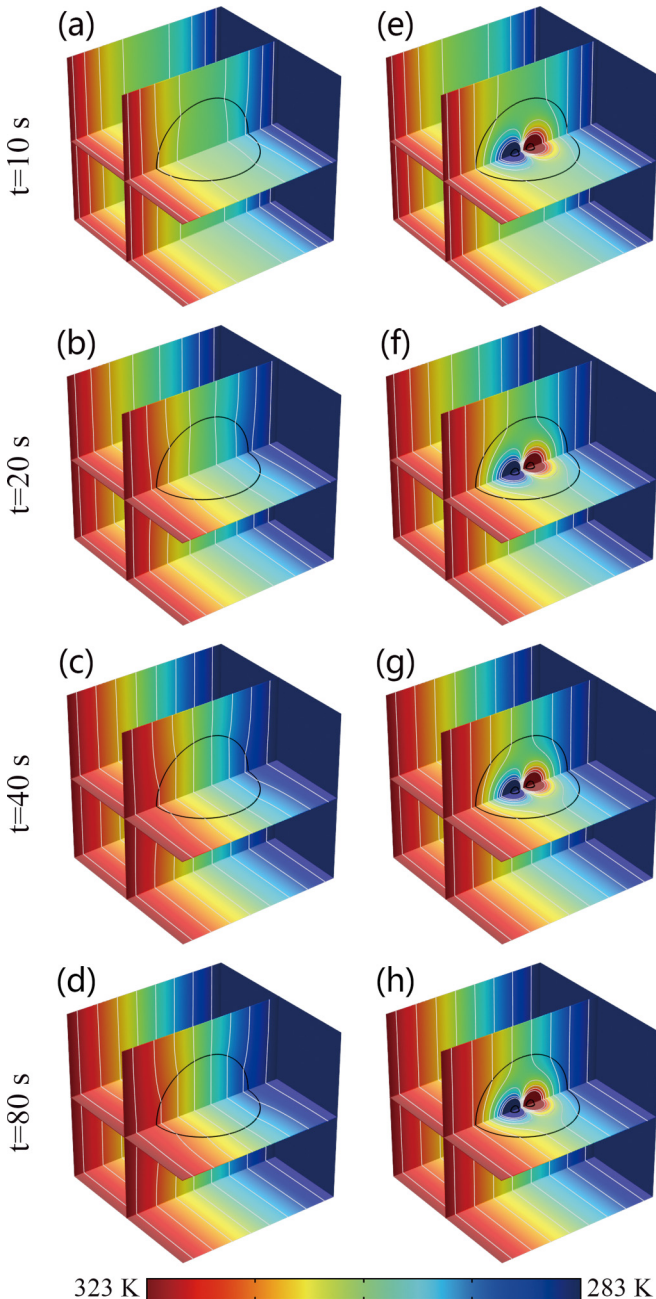
FIG. 7. Transient finite-element simulations based on Fig. 6(a): results (a–d) without and (e–h) with the thermal dipole, respectively. The initial temperature is set at 303 K. The density and the heat capacity of the particle and the matrix are 8960 kg m^{-3} and 385 J kg^{-1} K^{-1}, respectively.

matrix temperature-difference distribution ($\Delta T' = T'_1 - T'_2$) to perform quantitative analyses [see Fig. 6(c)]. The maximum value of the temperature difference ($\Delta T'_{\max}$) is 0.07 K. Compared with the temperature difference between the hot and cold sources ($\Delta T'_0 = 40$ K), the relative error ($\Delta T'_{\max}/\Delta T'_0$) is 0.18%, which exhibits the good performance of the thermal dipole.

We also show the transient results of thermal invisibility in three dimensions (see Fig. 7). Figures 7(a)–7(d) are references without a thermal dipole. Certainly, the particle in the center is detectable due to the distorted matrix isotherms. However, the straight matrix isotherms in Figs. 7(e)–7(h) demonstrate that the thermal dipole works indeed.

VII. CONCLUSION

The dipole-driven scheme has shown the flexibility and superiority in thermal management, and potential applications can be expected in infrared signature reduction. For example, if there is an impurity (with different thermal conductivity from the matrix) in a system, it will distort the infrared signature. After applying the dipole-driven scheme, the distortion could be reduced to ensure a pure infrared signature. Thermal dipoles may also be used to realize other thermal phenomena beyond invisibility, such as thermal camouflage [21–27], and exhibit novel properties in complex systems such as thermal Janus structures [28] and many-particle systems [29,30]. Moreover, the properties of thermal quadrupoles may contain other interesting points. Last but not least, although the dipole-driven scheme is at the macroscale, it may also be extended to the nanoscale [31–33].

In summary, we have established the theory of dipole-assisted thermotics. This theory helps to realize dipole-driven thermal invisibility by tailoring the thermal dipole moment. The dipole-driven scheme removes the requirements of singular and uncommon thermal conductivities, which contribute to both practical applications and further developments of thermal metamaterials. The theoretical analyses are validated by both finite-element simulations and laboratory experiments. Potential applications can be expected in infrared signature reduction, simplification of thermal metamaterials, etc.

ACKNOWLEDGMENTS

[1] C. Z. Fan, Y. Gao, and J. P. Huang, Shaped graded materials with an apparent negative thermal conductivity, Appl. Phys. Lett. **92**, 251907 (2008).

[2] T. Y. Chen, C. N. Weng, and J. S. Chen, Cloak for curvilinearly anisotropic media in conduction, Appl. Phys. Lett. **93**, 114103 (2008).

[3] S. Narayana and Y. Sato, Heat Flux Manipulation with Engineered Thermal Materials, Phys. Rev. Lett. **108**, 214303 (2012).

[4] Y. Li, X. Y. Shen, Z. H. Wu, J. Y. Huang, Y. X. Chen, Y. S. Ni, and J. P. Huang, Temperature-Dependent Transformation Thermotics: From Switchable Thermal Cloaks to Macroscopic Thermal Diodes, Phys. Rev. Lett. **115**, 195503 (2015).

[5] Y. Li, X. Bai, T. Z. Yang, H. Luo, and C. W. Qiu, Structured thermal surface for radiative camouflage, Nat. Commun. **9**, 273 (2018).

[6] H. Y. Xu, X. H. Shi, F. Gao, H. D. Sun, and B. L. Zhang, Ultrathin Three-Dimensional Thermal Cloak, Phys. Rev. Lett. **112**, 054301 (2014).

[7] T. C. Han, X. Bai, D. L. Gao, J. T. L. Thong, B. W. Li, and C. W. Qiu, Experimental Demonstration of a Bilayer Thermal Cloak, Phys. Rev. Lett. **112**, 054302 (2014).

[8] Y. G. Ma, Y. C. Liu, M. Raza, Y. D. Wang, and S. L. He, Experimental Demonstration of a Multiphysics Cloak: Manipulating Heat Flux and Electric Current Simultaneously, Phys. Rev. Lett. **113**, 205501 (2014).

[9] T. C. Han, X. Bai, J. T. L. Thong, B. W. Li, and C. W. Qiu, Full control and manipulation of heat signatures: Cloaking, camouflage and thermal metamaterials, Adv. Mater. **26**, 1731 (2014).

[10] T. C. Han, P. Yang, Y. Li, D. Y. Lei, B. W. Li, K. Hippalgaonkar, and C. W. Qiu, Full-parameter omnidirectional thermal metadevices of anisotropic geometry, Adv. Mater. **30**, 1804019 (2018).

[11] L. J. Xu and J. P. Huang, Metamaterials for manipulating thermal radiation: Transparency, cloak, and expander, Phys. Rev. Appl. **12**, 044048 (2019).

[12] X. He and L. Z. Wu, Thermal transparency with the concept of neutral inclusion, Phys. Rev. E **88**, 033201 (2013).

[13] L. W. Zeng and R. X. Song, Experimental observation of heat transparency, Appl. Phys. Lett. **104**, 201905 (2014).

[14] T. Z. Yang, X. Bai, D. L. Gao, L. Z. Wu, B. W. Li, J. T. L. Thong, and C. W. Qiu, Invisible sensors: Simultaneous sensing and camouflaging in multiphysical fields, Adv. Mater. **27**, 7752 (2015).

[15] Y. Li, K. J. Zhu, Y. G. Peng, W. Li, T. Z. Yang, H. X. Xu, H. Chen, X. F. Zhu, S. H. Fan, and C. W. Qiu, Thermal meta-device in analogue of zero-index photonics, Nat. Mater. **18**, 48 (2018).

[16] D. M. Nguyen, H. Y. Xu, Y. M. Zhang, and B. L. Zhang, Active thermal cloak, Appl. Phys. Lett. **107**, 121901 (2015).

[17] J. Guo and Z. G. Qu, Thermal cloak with adaptive heat source to proactively manipulate temperature field in heat conduction process, Int. J. Heat Mass Transfer **127**, 1212 (2018).

[18] J. B. Pendry, D. Schurig, and D. R. Smith, Controlling electromagnetic fields, Science **312**, 1780 (2006).

[19] L. J. Xu, S. Yang, and J. P. Huang, Designing effective thermal conductivity of materials of core-shell structure: Theory and simulation, Phys. Rev. E **99**, 022107 (2019).

[20] COMSOL MULTIPHYSICS, http://www.comsol.com.

[21] L. J. Xu, R. Z. Wang, and J. P. Huang, Camouflage thermotics: A cavity without disturbing heat signatures outside, J. Appl. Phys. **123**, 245111 (2018).

[22] X. He and L. Z. Wu, Illusion thermodynamics: A camouflage technique changing an object into another one with arbitrary cross section, Appl. Phys. Lett. **105**, 221904 (2014).

[23] T. Z. Yang, Y. Su, W. Xu, and X. D. Yang, Transient thermal camouflage and heat signature control, Appl. Phys. Lett. **109**, 121905 (2016).

[24] R. Hu, S. L. Zhou, Y. Li, D. Y. Lei, X. B. Luo, and C. W. Qiu, Illusion thermotics, Adv. Mater. **30**, 1707237 (2018).

[25] S. L. Zhou, R. Hu, and X. B. Luo, Thermal illusion with twinborn-like heat signatures, Int. J. Heat Mass Transfer **127**, 607 (2018).

[26] L. J. Xu, S. Yang, and J. P. Huang, Passive Metashells with Adaptive Thermal Conductivities: Chameleonlike Behavior and its Origin, Phys. Rev. Appl. **11**, 054071 (2019).

[27] R. Hu, S. Y. Huang, M. Wang, X. L. Luo, J. Shiomi, and C. W. Qiu, Encrypted thermal printing with regionalization transformation, Adv. Mater. **31**, 1807849 (2019).

[28] L. J. Xu, S. Yang, and J. P. Huang, Thermal theory for heterogeneously architected structure: Fundamentals and application, Phys. Rev. E **98**, 052128 (2018).

[29] J. X. Li, Y. Li, T. L. Li, W. Y. Wang, L. Q. Li, and C. W. Qiu, Doublet Thermal Metadevice, Phys. Rev. Appl. **11**, 044021 (2019).

[30] L. J. Xu, S. Yang, and J. P. Huang, Thermal Transparency Induced by Periodic Interparticle Interaction, Phys. Rev. Appl. **11**, 034056 (2019).

[31] J. Ren, P. Hanggi, and B. W. Li, Berry-Phase-Induced Heat Pumping and Its Impact on the Fluctuation Theorem, Phys. Rev. Lett. **104**, 170601 (2010).

[32] J. Ren, S. Liu, and B. W. Li, Geometric Heat Flux for Classical Thermal Transport in Interacting Open Systems, Phys. Rev. Lett. **108**, 210603 (2012).

[33] N. B. Li, J. Ren, L. Wang, G. Zhang, P. Hanggi, and B. W. Li, *Colloquium*: Phononics: Manipulating heat flow with electronic analogs and beyond, Rev. Mod. Phys. **84**, 1045 (2012).